optica

Broadband thermomechanically limited sensing with an optomechanical accelerometer

Feng Zhou,[1,2] Yiliang Bao,[1,2] Ramgopal Madugani,[1] David A. Long,[1] Jason J. Gorman,[1,3] and Thomas W. LeBrun[1,4]

[1]National Institute of Standards and Technology, 100 Bureau Drive, Gaithersburg, Maryland 20899, USA
[2]Theiss Research, La Jolla, California 92037, USA
[3]e-mail: gorman@nist.gov
[4]e-mail: lebrun@nist.gov

Received 22 October 2020; revised 27 January 2021; accepted 27 January 2021 (Doc. ID 413117); published 9 March 2021

Acceleration measurement is widely used in commercial, scientific, and defense applications, but the resolution and accuracy achievable for demanding applications is limited by the current technology used to build and calibrate accelerometers. We report an optomechanical accelerometer based on a Fabry–Perot microcavity in a silicon chip that is extremely precise, field deployable, and can self-calibrate. The measured acceleration resolution is the highest reported to date for a microfabricated optomechanical accelerometer and is achieved over a wide frequency range ($314\ \mathrm{nm\cdot s^{-2}/\sqrt{Hz}}$ over 6.8 kHz). The combination of a single vibrational mode in the mechanical spectrum and the broadband thermally limited resolution enables accurate conversion from sensor displacement to acceleration. This also allows measurement of acceleration directly in terms of the laser wavelength, making it possible for sensors to calibrate internally and serve as intrinsic standards. This sensing platform is applicable to a range of measurements from industrial accelerometry and inertial navigation to gravimetry and fundamental physics.

https://doi.org/10.1364/OPTICA.413117

1. INTRODUCTION

High-precision, high-bandwidth acceleration measurement is central to many important applications, including inertial navigation [1,2], seismometry [3,4], and structural health monitoring of buildings and bridges [5]. Traditional electromechanical accelerometers have largely relied on piezoelectric, capacitive, or piezoresistive transduction to convert the displacement of the accelerometer's proof mass to an output voltage when an excitation is applied. However, these transduction methods have reached sensitivity and bandwidth limits that are prohibitive for many applications. As a result, optical accelerometers have long been of interest due to the high precision provided by interferometry. These have included accelerometers assembled from macroscale optics [6] as well as those based on fiber optic interferometers [7] and fiber Bragg grating cavities [8]. More recently, cavity optomechanics has opened new avenues of research in both fundamental physics and precision measurement [9] by significantly advancing the sensitivity achievable in detecting attonewton forces [10], magnetic fields [11], and gravitational waves [12]. The development of integrated micro- and nanoscale optomechanical devices has produced accelerometers with significantly better displacement resolution than previously reported. Examples include a zipper photonic crystal optomechanical cavity in silicon nitride [13], a fiber-based microcavity integrated into a fused silica mechanical resonator [14,15], a whispering-gallery-mode accelerometer [16], and a slot-type photonic crystal cavity [17]. These integrated micro- and nanoscale cavities provide displacement resolution in the range of $1\ \mathrm{fm/\sqrt{Hz}}$ and below due to their low optical loss, which can result in an acceleration resolution on the order of $1\ \mathrm{\mu m\cdot s^{-2}/\sqrt{Hz}}$ and below for acceleration frequencies up to 10 kHz or more [13–17].

In addition to high resolution, optomechanical accelerometers promise greater accuracy without the need for calibration because the displacement of the proof mass can be measured directly in terms of the laser wavelength, an accepted practical realization of the meter [18], rather than electrical quantities. To determine the acceleration acting on the sensor from the displacement of its proof mass, the device physics must be accurately known. Therefore, the accelerometer must have a simple, deterministic mechanical response so that the dynamic model can be accurately inverted to convert displacement to acceleration. Ideally, the thermomechanical noise of the accelerometer should exceed the other fundamental noise source, optical shot noise in the displacement measurement, so that the mechanical response can be identified with high fidelity and the acceleration noise floor will be flat over a wide frequency range [19–21].

In previous work, the mechanical mode structure has been too complex and difficult to identify to allow reliable, broadband conversion between displacement and acceleration, or shot noise has dominated over most of the bandwidth of the accelerometer, or both, thereby preventing broadband measurement. Here we demonstrate a microfabricated optomechanical accelerometer that reaches the thermodynamic resolution limit over a broad

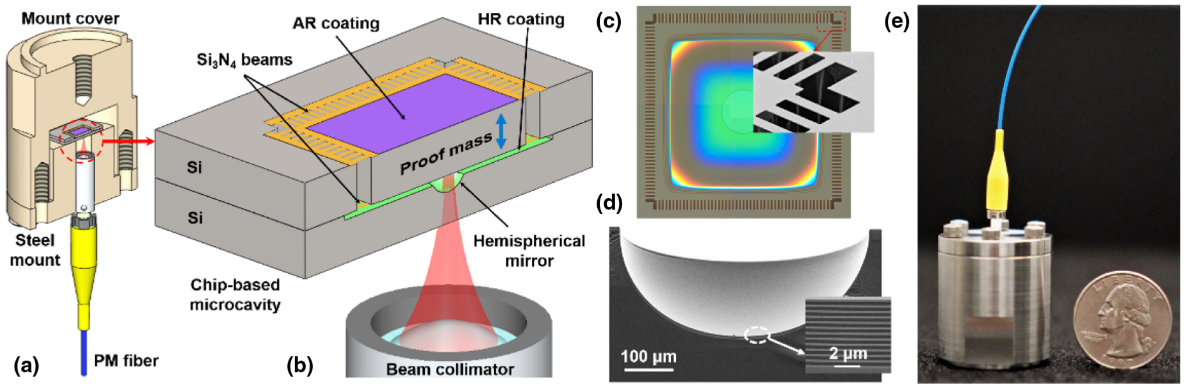

Fig. 1. Optomechanical accelerometer design. (a) Cross section of the accelerometer, including microfabricated cavity optomechanical components, polarization maintaining (PM) fiber optics, and a stainless-steel package. (b) Cross section of the two microfabricated chips. (c) Stitched optical micrograph of the mechanical resonator showing the high-reflectivity mirror coating restricted to the proof mass in order to avoid fouling the microbeams. Inset: Scanning electron micrograph of the silicon nitride microbeams. (d) Scanning electron micrograph of a cleaved concave silicon micromirror. Inset: Close-up of the high-reflectivity mirror coating with quarter-wave periodicity. (e) Image of a packaged and fiber-coupled accelerometer.

frequency range ($314\,\mathrm{nm}\cdot\mathrm{s}^{-2}/\sqrt{\mathrm{Hz}}$ over 6.8 kHz), greatly exceeding the resolution and bandwidth found in conventional accelerometers. Broadband measurement is necessary for detection of general time-varying signals at the thermodynamic limit, as well as rigorous understanding of the device physics required for advanced applications. In addition, the devices reported here are fully packaged, field-deployable, scalable, operable in air and vacuum—and achieve the highest acceleration resolution reported to date for a microfabricated optomechanical accelerometer. While the focus here is acceleration for vibration measurement, the platform is equally well suited for inertial sensing, seismometry, and gravimetry. In addition, the platform is applicable to many other applied and fundamental physical measurements. For example, optomechanical detection has recently been applied to dark matter detection [22], and approaches using mechanical detection have been proposed that include geometries similar to that presented here [23–25].

2. ACCELEROMETER DESIGN

The optomechanical accelerometer and its components are described in Fig. 1. Two silicon microfabricated chips comprise the main sensing elements of the accelerometer. One chip contains a millimeter-scale silicon proof mass suspended on both sides by silicon nitride (Si_3N_4) microbeams, and the other chip has a concave silicon micromirror. Both optical elements have patterned dielectric mirror and antireflective coatings. A hemispherical Fabry–Perot cavity is formed by assembling the chips such that the displacement of the mechanical resonator relative to the concave micromirror can be measured with high precision by interrogating one of the cavity's optical resonances [Fig. 1(b)]. When an acceleration is applied to the accelerometer package, the mechanical resonator displaces relative to the concave micromirror, which is measured as an intensity change in the light reflected from the cavity and converted to a measured acceleration.

The concave micromirror is fabricated in single crystal silicon using a wet etching process [26,27], resulting in high-quality mirrors with radii of curvature of approximately 410 μm, a depth of 257 μm, and a surface roughness of 1 nm RMS. The mechanical resonator is composed of a single-crystal silicon proof mass that is constrained on both sides by 1.5 μm thick silicon nitride beams [Fig. 1(c)]. This design ensures nearly ideal piston-like displacement in response to an acceleration perpendicular to the chip's surface and provides large frequency separation between the piston mode and higher-order modes (see Supplement 1). In addition, this design provides low cross-axis sensitivity because the in-plane stiffness of the resonator is 1700 times larger than that along the optical axis based on finite element analysis.

Two accelerometers were used in the presented experiments, which are only principally different in the dimensions of the proof mass and silicon nitride beams as well as the packaging. Device A has a 3 mm × 3 mm × 0.525 mm proof mass; beams that are 20 μm wide, 92 μm long, and spaced by 20 μm; a resonant frequency of 9.86 kHz; a mass of approximately 11 mg; and it is packaged as shown in Fig. 1(e). Device B is a bare device mounted without a cover for vacuum compatibility and has a 4 mm × 4 mm × 0.525 mm proof mass; beams that are 20 μm wide, 84 μm long, and spaced by 20 μm; a resonant frequency of 8.74 kHz; and a mass of approximately 20 mg. This sensor design can be extended to a range of measurements such as force, pressure, seismology, and gravimetry by simply modifying the mechanical resonator to have the appropriate mass, stiffness, and damping properties for the given application.

3. ACCELEROMETER FABRICATION AND ASSEMBLY

The concave silicon micromirror was fabricated using a slow isotropic wet etching process on a double-side polished, 525 μm thick silicon wafer. First, a 35 μm deep recess was etched using deep reactive ion etching (DRIE), providing space between the moving proof mass and micromirror when assembled. Then the wafer was coated with stoichiometric silicon nitride (300 nm thick) using low-pressure chemical vapor deposition (LPCVD), which serves as a hard mask during wet etching. Circular apertures 300 μm in diameter were patterned in the silicon nitride layer using reactive ion etching (RIE). The wafer was then etched in a mixture of hydrofluoric, nitric, and acetic acids (HNA, 9:75:30 ratio) at room temperature for a predetermined time to achieve the desired depth and radius of curvature, which are approximately 257 μm and 410 μm, respectively, in the presented accelerometers. See [27] for more details.

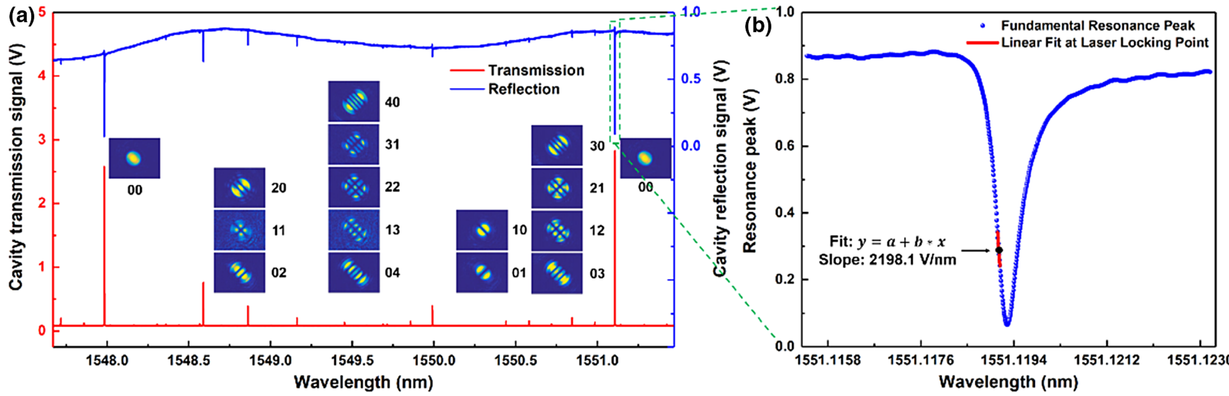

Fig. 2. Spectra for the optical cavity. (a) Reflected and transmitted spectra for the optical cavity over a single free spectral range (FSR) near 1550 nm. Higher-order transverse modes in addition to the fundamental (TEM_{00}) modes are imaged in transmission using an InGaAs camera. (b) A single fundamental mode that is used to transduce the motion of the proof mass is shown, where the optical finesse F is 5430. The red region on the resonance indicates the location for side-locking to the cavity.

The mechanical resonator was fabricated on a double-side polished, 525 μm thick silicon wafer by patterning both sides of the wafer identically. A 1.5 μm thick, low-stress silicon nitride layer was deposited on the wafer using LPCVD. The proof mass and beam geometry were patterned with optical lithography, and the silicon nitride was etched with RIE. DRIE was then used to etch the beam pattern through the silicon wafer from both sides in subsequent etch steps. After dicing into 1 cm chips, the beams and proof mass were released by undercutting the silicon nitride beams using KOH with a concentration of 30% at 60°C. The anisotropic etch results in a uniform, faceted sidewall on the proof mass that is self-limiting due to the etch resistance of the ⟨111⟩ crystal planes, providing repeatable dimensions for the proof mass.

Dielectric mirror and antireflection coatings with alternating tantalum pentoxide and silicon dioxide layers were applied to the concave micromirrors and mechanical resonators using ion beam sputtering [Fig. 1(d)]. A shadow mask made from an etched silicon wafer was used to selectively deposit the coatings on the proof mass and concave mirror. A pair of the completed chips were aligned and bonded with UV curable adhesive. This is a self-aligned process that requires no adjustment of angle or translation beyond ensuring overlap of the concave micromirror and proof mass. Finally, the chip assembly was aligned to a polarization maintaining fiber collimator within the accelerometer package and bonded using UV curable adhesive [Fig. 1(a)]. Antireflection coatings on the focusing lens and the back of the proof mass are used to reduce parasitic reflections.

4. OPTICAL READOUT

The optical spectrum of the hemispherical cavity was measured in both transmission and reflection as shown for wavelengths near 1550 nm in Fig. 2(a), where the free spectral range (FSR) is 400 GHz (3.21 nm), and higher-order transverse modes can be seen between the dominant fundamental modes. These modes were imaged in transmission on an InGaAs camera, showing intensity profiles characteristic of highly symmetric spatial modes. Modes grouped in columns have similar resonance wavelengths but are not degenerate. Displacement measurements of the mechanical resonator were performed in reflection using a fundamental cavity mode (TEM_{00}) near a wavelength of 1551 nm with a linewidth of $\Gamma = 73.7$ MHz (FWHM), a finesse of $F = 5430$, and a mirror reflectivity of $R = 99.89\%$ as shown in Fig. 2(b). The selection of F was based on the trade-off between sensitivity and dynamic range for measurement with a side-locked laser.

The readout method used for small-amplitude displacement measurement of the optical cavity is shown in Fig. 3(a). A stable fiber laser (FL) with a short-term linewidth near 100 Hz is phase modulated using an electro-optic modulator (EOM), which is driven near 3 GHz to generate sidebands. One sideband is locked to the cavity at the maximum slope point on the side of the optical resonance. Side-locking is achieved with a low bandwidth proportional-integral-derivative (PID) controller (≈ 300 Hz). Slow changes in cavity length, largely due to thermal- or humidity-induced drift of the cavity length, are tracked by the laser wavelength, while faster motion of the mechanical resonator generates intensity fluctuations that are used to detect acceleration. The incident optical power is 350 μW, which is expected to displace the proof mass by roughly 100 fm on resonance due to radiation pressure. Though a measurable displacement, this does not affect the results reported here. A static displacement does not change the response function of the accelerometer, which depends only on the resonant frequency and damping.

To suppress laser intensity noise, a balanced detection scheme with a bandwidth near 1 MHz was used. The resulting signal from the balanced detector was digitized using a 12-bit spectrum analyzer with a bandwidth of 28 kHz. This approach was used for the sensing resolution measurements presented in Section 5 due to the superior broadband noise performance of the FL. In addition, a widely tunable external cavity diode laser (ECDL) was used in place of the FL for the measurements in this section and in Section 6 due to its wider wavelength tuning range and resulting ability to easily tune to a desired cavity mode under rapidly varying measurement conditions (see Supplement 1). For both lasers, the reflected intensity fluctuations for the side-locked cavity result in a detector voltage ΔV that is converted to displacement ΔL using the relation $\Delta L = L\,\Delta V/(\lambda\,S)$, where L is the nominal cavity length, λ is the nominal cavity resonance wavelength, and $S = dV/d\lambda$ is the slope of the optical resonance at the lock point (see details in Supplement 1).

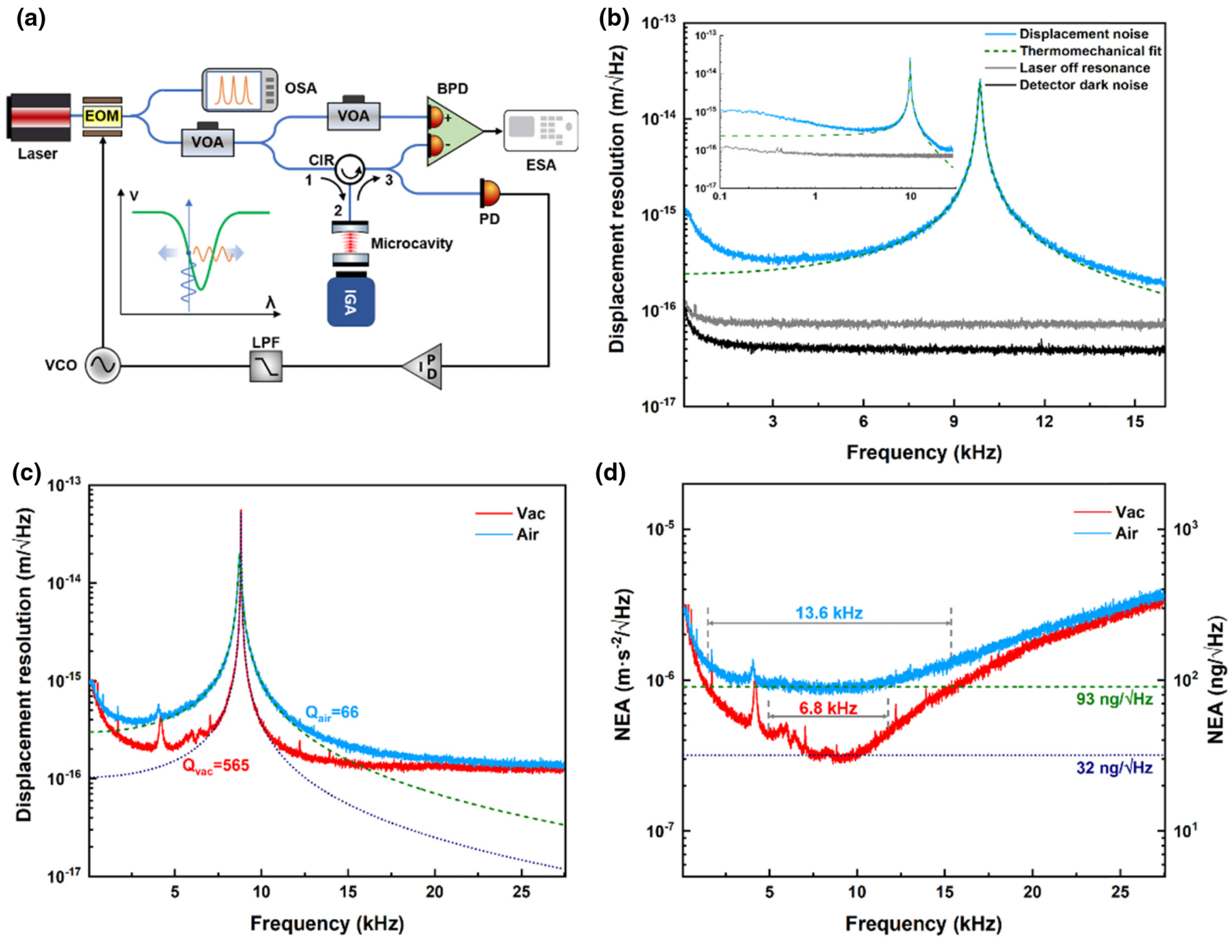

Fig. 3. Displacement spectral densities and the noise equivalent acceleration. (a) Diagram of the optical cavity readout method used to measure the noise performance of the accelerometer. EOM, electro-optic phase modulator; VOA, variable optical attenuator; OSA, optical spectrum analyzer; VCO, voltage-controlled oscillator; CIR, circulator; BPD, balanced photodetector; ESA, electronic spectrum analyzer; IGA, InGaAs camera; PD, photodetector; LPF, low-pass filter; and PID, proportional-integral-derivative controller. (b) Displacement spectral density for the accelerometer in air. Dashed line: Fit to the thermomechanical noise model. Gray line: Shot noise when the laser sideband is completely detuned from the optical resonance. Black line: Photodetector dark noise. Inset: Log–log plot of displacement spectral density. (c) Comparison between operation in air and in vacuum. Dashed lines: Respective fits to the thermomechanical noise model. (d) Noise equivalent acceleration (NEA). Indicated frequency bands represent the range over which the NEA is within 3 dB of the acceleration thermomechanical noise limit (dashed lines).

5. SENSING RESOLUTION

The displacement noise floor was measured in air and in a vacuum chamber ($P = 133$ mPa) at room temperature, while the accelerometer was acoustically and vibrationally isolated. The resulting displacement spectral density in air for Device A is shown in Fig. 3(b), where a single vibrational mode is present between 100 Hz and 28 kHz and is driven purely by thermomechanical noise. This is the first demonstration reported of an optomechanical accelerometer operating with a single vibrational mode over such a wide bandwidth. A pure single-mode response is important for the accurate determination of the acceleration acting on the sensor from the displacement of its proof mass using first principles (see Supplement 1). The presence of additional modes and antiresonances between modes would increase the complexity of the model fit from the thermomechanical noise response. In addition, antiresonances are generally not visible in the thermomechanical noise response. Both of these issues can result in significant inaccuracy in the conversion from displacement to acceleration with a multimode model.

A fit of the displacement spectral density to the expected thermomechanical noise response for a simple harmonic oscillator with viscous damping shows close agreement in Fig. 3(b) (see Supplement 1), allowing precise estimates of the resonance frequency $\omega_0 = 2\pi \times 9.852(16)$ kHz, quality factor $Q = 99(2)$, and mass $m = 10.8(9)$ mg. This mass estimate derived from the thermomechanical fit is well within the uncertainty of the value of 11.07(53) mg calculated from the dimensions of the silicon resonator and optical coatings (see Supplement 1). The noise floor at the lowest frequencies is set by readout noise that is likely due to laser frequency noise, phase modulation noise from the EOM, or thermal effects. Well above resonance, approaching 28 kHz, the noise floor closely approaches the optical shot noise limit. Importantly, the displacement resolution is limited by thermomechanical noise over most of the measured frequency range. This was achieved by optimizing the optical (L, F) and mechanical (m, Q, ω_0) parameters so that the thermomechanical noise is above or equal to the shot noise within the bandwidth of interest. One benefit of being broadband limited by thermomechanical noise is that the harmonic oscillator model fit can be very accurate due to a high signal-to-noise ratio, which provides greater precision when converting from proof mass displacement to acceleration.

Comparing the displacement spectral density in air and vacuum for Device B in Fig. 3(c), the increased Q in vacuum, due to a reduction in gas damping, results in larger thermomechanical noise on resonance and less away from resonance, as expected. However, due to the balance between the thermomechanical noise and shot noise, the frequency range over which the spectral density is thermomechanically limited is clearly reduced. The displacement spectral densities in Fig. 3(c) are converted to a noise equivalent acceleration (NEA) by dividing the response by the harmonic oscillator transfer function (see Supplement 1) as shown in Fig. 3(d). As expected, the NEA reaches the acceleration thermomechanical limit, which is independent of frequency ($a_{\text{th}} = \sqrt{4k_B T\omega_0/mQ}$, see Supplement 1), wherever the displacement spectral density is limited by thermomechanical noise. Fluctuations are reduced when the damping is lower, providing a lower thermodynamic limit but making it more difficult to reach since the shot noise must be lower than the thermomechanical noise. Due to increased damping in air, the minimum NEA is higher, $912\ \text{nm}\cdot\text{s}^{-2}/\sqrt{\text{Hz}}$ ($93\ \text{ng}_n/\sqrt{\text{Hz}}$, $1\ \text{g}_n = 9.81\ \text{m}\cdot\text{s}^{-2}$), than in vacuum, $314\ \text{nm}\cdot\text{s}^{-2}/\sqrt{\text{Hz}}$ ($32\ \text{ng}_n/\sqrt{\text{Hz}}$). The resolution in vacuum represents the lowest value reported—by 2 orders of magnitude—for a microfabricated optomechanical accelerometer with equivalent bandwidth [13,17]. The achieved resolution is significant in this class of device because microfabrication enables scalable fabrication and embedded devices. The bandwidth over which the NEA is within 3 dB of the acceleration thermomechanical limit is 13.6 kHz and 6.8 kHz for air and vacuum, respectively. This wide range is made possible by the exceptionally low displacement readout noise. Furthermore, the NEA only varies by 1 order of magnitude over the frequency range, which is an improvement of 2 to 4 orders of magnitude compared to previously reported optomechanical accelerometers [13,14]. This reasonably flat NEA is important for making high-precision broadband acceleration measurements since it provides a consistent signal-to-noise ratio over the measurement bandwidth.

6. SENSING PERFORMANCE UNDER EXTERNAL ACCELERATION

As a test of sensing performance for a range of external acceleration frequencies, the optomechanical accelerometer was placed on a piezoelectric shaker table, and the accelerometer output was compared with the motion measured with a homodyne Michelson interferometer [see Fig. 4(a) and Supplement 1]. The frequency of the sinusoidal acceleration generated by the shaker was swept from 1 to 20 kHz. The interferometer was used to measure the displacement of the accelerometer package, which has a 5 mm square gold-on-silicon mirror bonded to it. The resulting displacement amplitude as a function of drive frequency for Device A is shown in Fig. 4(b), where the displacement of the proof mass and package are different because the accelerometer response includes the resonance of the proof mass (9.86 kHz) and the first resonance of the shaker (12.68 kHz), whereas the external interferometer can only detect the shaker resonance. The inset shows that the shaker linearity is better than 1.3% (see Supplement 1). In addition to the large resonances, much smaller structures in the accelerometer displacement data can be seen at 3.9 kHz and 11.6 kHz. They have been linked to the accelerometer packaging and the shaker itself and are

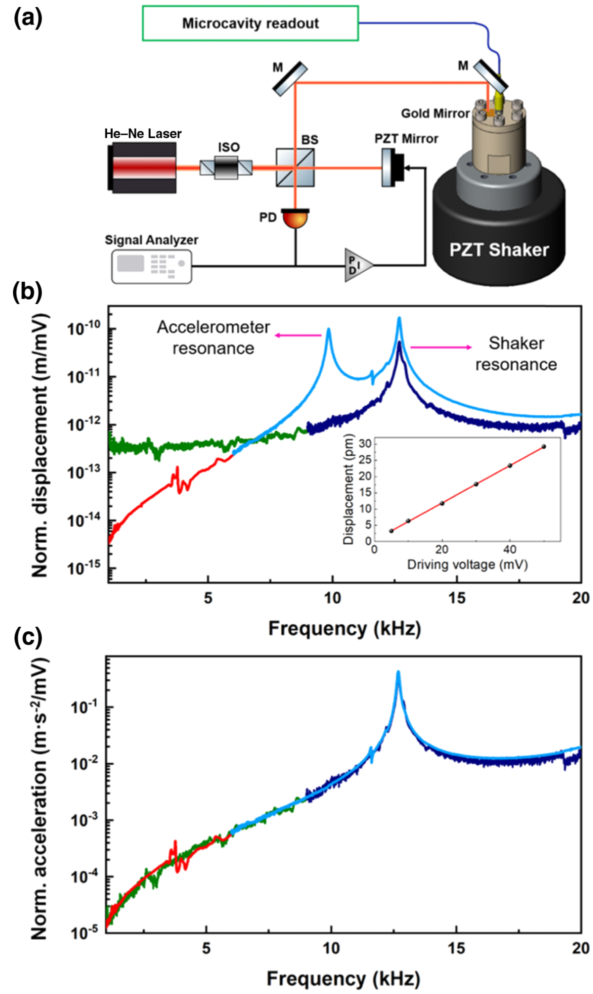

Fig. 4. Shaker table testing of the accelerometer. (a) Experimental configuration for the shaker table tests. M, mirror; PD, photodetector; BS, nonpolarizing beamsplitter; ISO, optical isolator; and PID, proportional-integral-derivative servo loop. The microcavity readout is shown in Fig. 3(a). (b) Comparison of the normalized displacement measured with the accelerometer and interferometer. (c) Comparison of the normalized acceleration measured by the accelerometer and interferometer. The displacement resolution of the accelerometer is more than 100 times greater than that of the interferometer ($0.1\ \text{fm}/\sqrt{\text{Hz}}$ and $60\ \text{fm}/\sqrt{\text{Hz}}$, respectively). As a result, different drive voltages were used, 0.1 mV (blue) and 25 mV (red) for the accelerometer and 5 mV (navy) and 30 mV (green) for the interferometer, respectively. The shaker was found to be highly linear for this drive voltage range [see the inset in (b) at a shaker frequency of 5 kHz and Supplement 1], making this comparison possible.

dependent on the torque used in mounting the accelerometer onto the shaker.

The displacement data from the accelerometer was converted to acceleration, and the interferometer displacement data was transformed to acceleration by multiplying by $(2\pi f_d)^2$, where f_d is the drive frequency. Each data set is normalized by the shaker table drive voltage. As shown in Fig. 4(c), there is close agreement between the accelerometer and interferometer throughout the entire 20 kHz bandwidth. The maximum amplitude of acceleration measured in this case is slightly less than $0.1\ \text{m/s}^2$. Using a side lock at higher amplitudes can lead to loss of lock or nonlinear response, so an optical comb readout for microcavities has been developed to measure larger amplitudes [28].

The accelerometer's fundamental resonance does not appear in the acceleration data due to the model inversion, demonstrating that measurement on and even above resonance can be effective for these single-mode devices. The percent deviation of the accelerometer from the interferometer was calculated at each measurement frequency. The standard deviation of this value over the entire frequency range is 15.9% and between 4.5 and 11 kHz it is 9.7% after applying a moving average filter to the interferometer data to reduce noise (see Supplement 1). This comparison confirms that the accelerometer is behaving like a harmonic oscillator (i.e., exhibiting a single, one-dimensional, viscously damped piston mode of the proof mass) and is effective for broadband acceleration measurements. This represents the widest bandwidth demonstrated to date at this error level using a first-principles description based on a single-degree-of-freedom oscillator model. However, this comparison does not accurately indicate the accelerometer performance, as the deviation is dominated by the mechanics of the external reference interferometer and its interaction with the shaker table.

7. CONCLUSION

In conclusion, we have demonstrated a compact, microfabricated optomechanical accelerometer that achieves the thermodynamic limit of resolution over a frequency range greater than 13 kHz, including on, above, and below resonance. Microfabrication enables scalable fabrication and embedded applications, while the highly ideal single-mode structure enables accurate inversion of the mechanical response for accurate measurement. Additionally, broadband measurement at the thermodynamic limit yields a detection resolution nearly independent of frequency, so resonant enhancement is not necessary for detection of weak signals and detection even above resonance is possible with the same noise-equivalent resolution despite a rapidly falling response. The compact size of the sensor enables high-precision measurements outside of laboratory settings, and the optomechanical sensing platform is widely applicable to measurements beyond acceleration, such as force, pressure, and gravity sensing, through straightforward modification of the mechanical resonator.

Funding. National Institute of Standards and Technology (NIST on a Chip Program, 70NANB17H247, 70NANB20H174).

Acknowledgment. This work was partially supported by the NIST on a Chip Program. Y. B. acknowledges support from the National Institute of Standards and Technology (NIST), Department of Commerce, USA (70NANB17H247). F. Z. acknowledges support from the National Institute of Standards and Technology (NIST), Department of Commerce, USA (70NANB20H174). The authors thank Ben Reschovsky for helpful discussions and sharing analysis of the uncertainties derived from fits to thermomechanical spectra. This research was performed in part in the NIST Center for Nanoscale Science and Technology NanoFab.

Disclosures. The authors declare no conflicts of interest.

Supplemental document. See Supplement 1 for supporting content.

REFERENCES

1. N. Yazdi, F. Ayazi, and K. Najafi, "Micromachined inertial sensors," Proc. IEEE **86**, 1640–1659 (1998).
2. D. K. Shaeffer, "MEMS inertial sensors: a tutorial overview," IEEE Commun. Mag. **51**(4), 100–109 (2013).
3. H. Nakstad and J. Kringlebotn, "Probing oil fields," Nat. Photonics **2**, 147–149 (2008).
4. R. P. Middlemiss, A. Samarelli, D. J. Paul, J. Hough, S. Rowan, and G. D. Hammond, "Measurement of the Earth tides with a MEMS gravimeter," Nature **531**, 614–617 (2016).
5. H. Jo, J. A. Rice, Jr., B. F. Spencer, and T. Nagayama, "Development of high-sensitivity accelerometer board for structural health monitoring," Proc. SPIE **7647**, 764706 (2010).
6. A. R. Nelson and G. R. Elion, "Optical accelerometer," U.S. patent 4,567,771 (4 February 1986).
7. A. D. Kersey, D. A. Jackson, and M. Corke, "High-sensitivity fibre-optic accelerometer," Electron. Lett. **18**, 559–561 (1982).
8. T. A. Berkoff and A. D. Kersey, "Experimental demonstration of a fiber Bragg grating accelerometer," IEEE Photon. Technol. Lett. **8**, 1677–1679 (1996).
9. M. Aspelmeyer, T. J. Kippenberg, and F. Marquardt, "Cavity optomechanics," Rev. Mod. Phys. **86**, 1391–1452 (2014).
10. E. Gavartin, P. Verlot, and T. J. Kippenberg, "A hybrid on-chip optomechanical transducer for ultrasensitive force measurements," Nat. Nanotechnol. **7**, 509–514 (2012).
11. M. Wu, N. L. Y. Wu, T. Firdous, F. F. Sani, J. E. Losby, M. R. Freeman, and P. E. Barclay, "Nanocavity optomechanical torque magnetometry and radiofrequency susceptometry," Nat. Nanotechnol. **12**, 127–131 (2017).
12. LIGO Scientific Collaboration and Virgo Collaboration, "Observation of gravitational waves from a binary black hole merger," Phys. Rev. Lett. **116**, 061102 (2016).
13. A. G. Krause, M. Winger, T. D. Blasius, Q. Lin, and Q. Painter, "A high-resolution microchip optomechanical accelerometer," Nat. Photonics **6**, 768–772 (2012).
14. F. G. Cervantes, L. Kumanchik, J. R. Pratt, and J. M. Taylor, "High sensitivity optomechanical reference accelerometer over 10 kHz," Appl. Phys. Lett. **104**, 221111 (2014).
15. O. Gerberding, F. G. Cervantes, J. Melcher, J. R. Pratt, and J. M. Taylor, "Optomechanical reference accelerometer," Metrologia **52**, 654–665 (2015).
16. Y. L. Li and P. F. Barker, "Characterization and testing of a micro-g whispering gallery mode optomechanical accelerometer," J. Lightwave Technol. **36**, 3919–3926 (2018).
17. Y. Huang, J. G. Flor Flores, Y. Li, W. Wang, D. Wang, N. Goldberg, J. Zheng, M. Yu, M. Lu, M. Kutzer, D. Rogers, D.-L. Kwong, L. Churchill, and C. W. Wong, "A chip-scale oscillation-mode optomechanical inertial sensor near the thermodynamical limits," Laser Photon. Rev. **14**, 1800329 (2020).
18. T. J. Quinn, "Practical realization of the definition of the metre, including recommended radiations of other optical frequency standards (2001)," Metrologia **40**, 103–133 (2003).
19. T. B. Gabrielson, "Mechanical-thermal noise in micromachined acoustic and vibration sensors," IEEE Trans. Electron Devices **40**, 903–909 (1993).
20. T. B. Gabrielson, "Fundamental noise limits for miniature acoustic and vibration sensors," J. Vib. Acoust. **117**, 405–410 (1995).
21. J. Cripe, N. Aggarwal, R. Lanza, A. Libson, R. Singh, P. Heu, D. Follman, G. D. Cole, N. Mavalvala, and T. Corbitt, "Measurement of quantum back action in the audio band at room temperature," Nature **568**, 364–367 (2019).
22. F. Monteiro, G. Afek, D. Carney, G. Krnjaic, J. Wang, and D. C. Moore, "Search for composite dark matter with optically levitated sensors," Phys. Rev. Lett. **125**, 181102 (2020).
23. D. Carney, G. Krnjaic, D. C. Moore, C. A. Regal, G. Afek, S. Bhave, B. Brubaker, T. Corbitt, J. Cripe, N. Crisosto, A. Geraci, S. Ghosh, J. G. E. Harris, A. Hook, E. W. Kolb, J. Kunjummen, R. F. Lang, T. Li, T. Lin, Z. Liu, J. Lykken, L. Magrini, J. Manley, N. Matsumoto, A. Monte, F. Monteiro, T. Purdy, C. J. Riedel, R. Singh, S. Singh, K. Sinha, J. M. Taylor, J. Qin, D. J. Wilson, and A. Geraci, "Mechanical quantum sensing in the search for dark matter," Quantum Sci. Technol. **6**, 024002 (2021).
24. A. A. Geraci, C. Bradley, D. Gao, J. Weinstein, and A. Derevianko, "Searching for ultralight dark matter with optical cavities," Phys. Rev. Lett. **123**, 031304 (2019).
25. D. Carney, A. Hook, Z. Liu, J. M. Taylor, and Y. Zhao, "Ultralight dark matter detection with mechanical quantum sensors," New J. Phys. (2021) in press.

26. M. Trupke, E. A. Hinds, S. Eriksson, E. A. Curtis, Z. Moktadir, E. Kukharenka, and M. Kraft, "Microfabricated high-finesse optical cavity with open access and small volume," Appl. Phys. Lett. **87**, 211106 (2005).
27. Y. Bao, F. Zhou, T. W. LeBrun, and J. J. Gorman, "Concave silicon micromirrors for stable hemispherical optical microcavities," Opt. Express **25**, 15493–15503 (2017).
28. D. A. Long, B. J. Reschovsky, F. Zhou, Y. Bao, T. W. LeBrun, and J. J. Gorman, "Electro-optic frequency combs for rapid interrogation in cavity optomechanics," Opt. Lett. **46**, 645–648 (2021).

Supplemental Document

optica

Broadband thermomechanically limited sensing with an optomechanical accelerometer: supplement

FENG ZHOU,[1,2] YILIANG BAO,[1,2] RAMGOPAL MADUGANI,[1] DAVID A. LONG,[1] JASON J. GORMAN,[1,3] AND THOMAS W. LEBRUN[1,4]

[1] *National Institute of Standards and Technology, 100 Bureau Drive, Gaithersburg, Maryland 20899, USA*
[2] *Theiss Research, La Jolla, California 92037, USA*
[3] *e-mail: gorman@nist.gov*
[4] *e-mail: lebrun@nist.gov*

Supplement DOI: https://doi.org/10.6084/m9.figshare.13664609

Parent Article DOI: https://doi.org/10.1364/OPTICA.413117

Broadband thermomechanically-limited sensing with an optomechanical accelerometer: supplemental document

FENG ZHOU,[1,2] YILIANG BAO,[1,2] RAMGOPAL MADUGANI,[1] DAVID A. LONG,[1] JASON J. GORMAN,[1,*] AND THOMAS W. LEBRUN[1,*]

[1]National Institute of Standards and Technology, 100 Bureau Drive, Gaithersburg, Maryland 20899 USA
[2]Theiss Research, La Jolla, California 92037, USA
*Corresponding authors: gorman@nist.gov, thomas.lebrun@nist.gov

S1. Harmonic Oscillator Model

A major benefit of the accelerometer described in the article is that its dynamic response closely follows that of a one-dimensional viscously-damped harmonic oscillator, making it possible to convert from measured proof mass displacement to an equivalent acceleration using a low-order model. In this section, we describe the harmonic oscillator model and the conversion between displacement and acceleration. Much of the analysis in this section and the next follows directly from the work of Gabrielson [S1] but is specifically focused towards the optomechanical accelerometer.

The harmonic oscillator model is described in Fig. S1, where a mass-spring-damper system is driven by a base excitation, x_e. A stochastic force, F_L, is also applied to the harmonic oscillator, which results in Brownian motion, generating thermomechanical displacement noise. The oscillator can be described by the following Langevin equation

$$m\ddot{x} + c\left(\dot{x} - \dot{x}_e\right) + k\left(x - x_e\right) = F_L \qquad \text{(S1)}$$

where m is the mass, k is the spring stiffness, c is the damping coefficient, and x is the displacement of the mass. Defining the change in optical cavity length, x_c, as $x_c = x - x_e$ and the base acceleration, a_e, as $a_e = \ddot{x}_e$ results in the model of interest:

$$\ddot{x}_c + \frac{\omega_0}{Q}\dot{x}_c + \omega_0^2 x_c = -a_e + \frac{F_L}{m} \qquad \text{(S2)}$$

where $\omega_0 = \sqrt{k/m}$, $\omega_0 = 2\pi f_0$, f_0 is the resonance frequency in the absence of damping, $Q = m\omega_0/c$, and Q is the quality factor.

The relationship between cavity displacement, x_c, and base acceleration, a_e, as a function of frequency, ω, can be determined from eq. (S2) by neglecting the Langevin force, F_L.

$$x_c\left(\omega\right) = \frac{-1}{\omega_0^2 - \omega^2 - i\dfrac{\omega_0\omega}{Q}} a_e\left(\omega\right) = G\left(i\omega\right)a_e\left(\omega\right) \qquad \text{(S3)}$$

The amplitude of a_e can then be written as

$$\left|a_e\left(\omega\right)\right| = \left|G\left(i\omega\right)\right|^{-1}\left|x_c\left(\omega\right)\right|, \qquad \text{(S4)}$$

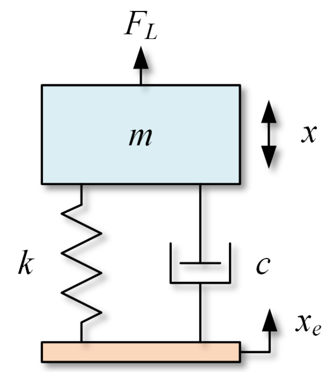

Fig. S1 Harmonic oscillator model described by a mass-spring-damper system. m: mass, k: spring stiffness, c: damping coefficient, x: proof mass displacement, x_e: base displacement, F_L: Langevin force.

which has been used to calculate the acceleration data in Figs. 3d and 4d in the article from displacement measurements. Implementing eq. (S4) requires measurement of ω_0 and Q. Here, this was done by applying a least-squares fit of $\left|G\left(i\omega\right)\right|$ to the data in Figs. 3b and 3c in the article.

S2. Thermomechanical and Optical Shot Noise

The stochastic force in the Langevin equation, eq. (S1), is defined as $F_L = \sqrt{4k_B T c}\,\Gamma\left(t\right)$, where k_B is Boltzmann's constant, T is temperature, and $\Gamma(t)$ is a Gaussian white noise process with a standard deviation of 1 [S1]. Returning to eq. (S2), ignoring a_e, and taking the power spectral density of x_c, defined as S_{xx}, results in

$$S_{xx}\left(\omega\right) = \left|G\left(i\omega\right)\right|^2 \frac{4k_B T\omega_0}{mQ} \qquad \text{(S5)}$$

The thermomechanical noise in terms of displacement is then defined as $x_{th} = S_{xx}\left(\omega\right)^{1/2}$, or

$$x_{th}\left(\omega\right) = \left|G\left(i\omega\right)\right|\sqrt{\frac{4k_B T\omega_o}{mQ}} \qquad \text{(S6)}$$

Recalling the conversion from displacement to acceleration, eq. (S4), the equivalent acceleration due to thermomechanical noise is then

$$a_{th} = \sqrt{\frac{4k_B T \omega_o}{mQ}} \tag{S7}$$

Interestingly, a_{th} is only a function of the resonator parameters (ω_0, m, and Q) and temperature, and not a function of frequency, meaning that the thermomechanical noise floor in terms of acceleration is flat.

In addition to thermomechanical noise, optical shot noise is the other fundamentally limiting noise source. The power spectral density of the optical shot noise is $S_{PP} = 2h\nu P_a/\eta$, where h is Planck's constant, ν is the optical frequency of the laser, P_a is the average power reaching the photodetector, and η is the quantum efficiency of the photodetector. This can be converted to shot noise in terms of displacement using

$$x_s = g_{x/V} g_{V/i} R\, S_{PP}^{1/2} = g_{x/V} g_{V/i} R \sqrt{2h\nu P_a/\eta} \tag{S8}$$

The gain $g_{x/V}$ converts photodetector voltage to displacement and is discussed in Section S4, while $g_{V/i}$ and R are the transimpedance gain and responsivity of the photodetector. Recalling eq. (S4), the shot noise in terms of acceleration is

$$a_s = g_{x/V} g_{V/i} R \sqrt{2h\nu P_a/\eta}\, \left|G(i\omega)\right|^{-1} \tag{S9}$$

Since the thermomechanical noise and shot noise are uncorrelated, they can be summed in quadrature to get the total noise equivalent displacement, x_{NE}, and acceleration, a_{NE}.

Unlike the thermomechanical displacement noise, x_{th}, the optical shot noise does not represent real resonator motion but rather, it is detection noise that is analytically referred to either displacement or acceleration. As a result, the best-case scenario for a resonator with fixed parameters (ω_0, Q, m, T) is for the optical shot noise to be lower than the thermomechanical noise. In this situation, the optical readout will measure the motion of the resonator with minimal contribution from shot noise. This is shown in Fig. S2, where the calculated noise floor is presented for a resonator with parameters similar to those described in the experiments in the article. Three different levels of shot noise are shown, where two are above the thermomechanical noise (dark blue, light blue) and one is below (red). When the shot noise is below the thermomechanical noise, the resonance shape is observed over the entire frequency range, which provide better estimates of ω_0 and Q when fitting displacement noise spectra to the harmonic oscillator model.

After converting the displacement to acceleration, as shown in Fig. S2b, the importance of reducing the shot noise is readily apparent. The noise equivalent acceleration is nearly flat over the frequency range when the shot noise is below the thermomechanical noise. Achieving a flat noise floor in acceleration is critical for a broadband accelerometer because it enables the measurement of signals with widely varying frequencies at the same precision level. For example, if the acceleration is a square wave, all of the harmonics within the bandwidth of the sensor will be measured with the same precision when the noise floor is flat, which means that the signal can be accurately reconstructed from the data. If the noise floor is frequency dependent, this reconstruction would be less accurate since the signal-to-noise ratio will vary across the frequency range.

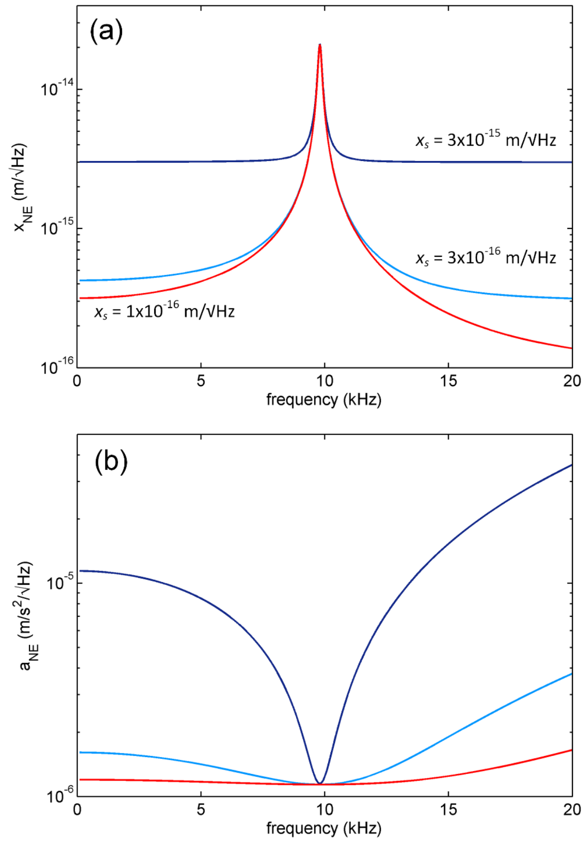

Fig. S2 Noise equivalent displacement and acceleration for varying optical shot noise level. (a) Noise equivalent displacement combining thermomechanical noise and optical shot noise at three different shot noise levels. ω_0 = 2π (9.8 kHz), Q = 70, m = 11 mg, T = 293 K. (b) Noise equivalent acceleration based on the displacement noise in (a).

S3. Design of the Mechanical Resonator

The mechanical resonator has a large square single-crystal silicon proof mass (thickness: 525 µm, width: 3.02 mm (Device A) or 4.02 mm (Device B)) that is supported by an array of 1.5 µm thick silicon nitride beams, as shown in Fig. 1 of the article. These beams are located around the entire perimeter of the proof mass and on both sides of the chip, where the beam length is selected to achieve the desired stiffness. This design increases the resonance frequencies for rotational modes of the proof mass (i.e., rocking modes) so that there is a large separation in frequency between the first translational mode (i.e., piston mode) and the other vibrational modes.

Structural finite element analysis (FEA) was performed for the two designs (Devices A and B) to assess the effectiveness

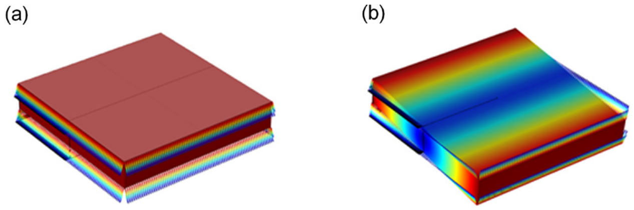

Fig. S3 Mode shapes for the mechanical resonator. (a) First piston mode, and (b) first rocking mode. Red indicates maximum displacement and dark blue represents no displacement.

of mode separation due to the flexural constraints. Figure S3 shows representative mode shapes for the first piston mode and first rocking mode. The piston mode is the mode of interest for detecting accelerations perpendicular to the chip surface. This mode exhibits pure translation of the proof mass along the optical axis, such that proof mass displacement causes a length change of the optical cavity. It was found that the resonance frequency of the first rocking mode is higher than the piston mode by a factor of 11.6 for Device A and 7.8 for Device B. This mode separation is sufficient to ensure that the rocking mode does not appear within the measurement bandwidth used for Fig. 3 in the article. The closest mechanical mode detected in experiments is above 60 kHz, or a factor of 6 higher than the piston mode, as shown in Fig. S4b.

S4. Converting from Photodetector Voltage to Displacement

Displacement of the proof mass results in a change in cavity length, which is measured by the cavity readout. With the probing laser locked to the side of a TEM_{00} optical resonance, the cavity length change, ΔL, is transduced by measuring the change in the center wavelength of the optical resonance, $\Delta\lambda$, using:

$$\Delta L = \frac{L}{\lambda}\Delta\lambda \qquad \text{(S10)}$$

where L is the nominal cavity length and λ is the nominal laser wavelength at the lock point. The change in the center wavelength, $\Delta\lambda$, is related to the reflected laser intensity from the cavity that is measured with a photodetector, resulting in a voltage change, ΔV. The relationship between voltage and wavelength is defined by the slope of the optical resonance at the locking point, $dV/d\lambda$, as shown in the inset of Fig. S4a. The laser was locked to the point of greatest slope for the highest transduction sensitivity. In this way, the displacement of the proof mass is found using:

$$\Delta L = \frac{L}{\lambda}\Delta V \Big/ \left(\frac{dV}{d\lambda}\right) = g_{x/V}\Delta V \qquad \text{(S11)}$$

The parameters (L, λ, $dV/d\lambda$) are directly found from a spectral measurement of the cavity over a full free spectral range (FSR) and the voltage change, ΔV, is measured with an electronic spectrum analyzer (ESA).

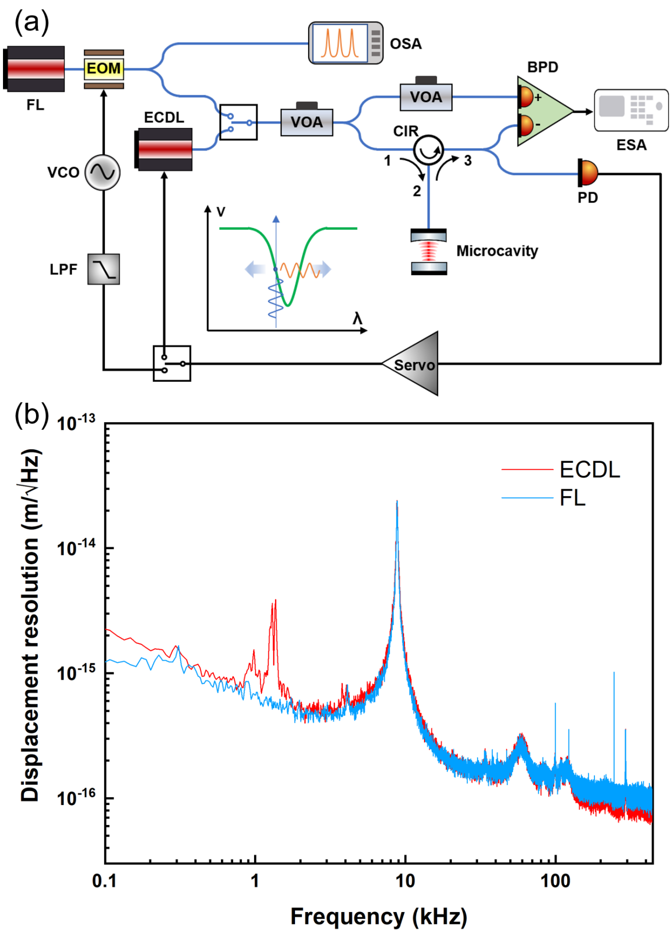

Fig. S4 Cavity readout with the external cavity diode laser. (a) Schematic of the cavity readout for the accelerometer using both the external cavity diode laser (ECDL) and fiber laser (FL). EOM: electro-optical modulator, SW: switch, OSA: optical spectrum analyzer; CIR: circulator, BPD: balanced photodetector, PD: photodetector, VOA: variable optical attenuator, ESA: electronic spectrum analyzer, LPF: low-pass filter, VCO: voltage-controlled oscillator. (b) Displacement noise spectra for the accelerometer when using the ECDL and FL.

S5. Readout Using the External Cavity Diode Laser

Two different lasers were used for cavity readout: a continuously tunable external cavity diode laser (ECDL) and a tunable fiber laser (FL) that is phase modulated with an electro-optic modulator (EOM). The ECDL has a wide wavelength tuning range and precise piezo-based wavelength control, allowing for cavity characterization and FSR measurements, as shown in Fig. 2 of the article. In comparison, the FL has a slow tuning rate and a much narrower tuning range. Furthermore, the internal feedback locking module of the ECDL enables direct and convenient cavity displacement readout. However, the ECDL has more internal frequency noise than the FL, which appears as noise equivalent displacement. Therefore, the FL was used for the displacement noise floor measurements in Fig. 3 of the article since it has a cleaner frequency spectrum. Details on the readout method using the FL are described in the article.

Here, we provide additional information on the readout with the ECDL.

As shown in Fig. S4a, the main differences between using the ECDL and FL are the wavelength tuning method and the feedback servo loop. Wavelength tuning with feedback is achieved in the ECDL with a piezoelectric actuator in the external cavity. Therefore, unlike the FL, an EOM is not needed for locking. Regarding the implementation of the servo, the ECDL has an internal digital proportional-integral-derivative (PID) feedback controller while the FL servo uses an external analog PID controller.

A comparison of the displacement noise spectra from the accelerometer is shown in Fig. S4b for both readout lasers. No mechanical resonances other than the fundamental near 10 kHz are observed in the accelerometer up to 60 kHz. In general, the responses from the two lasers are very similar. However, the ECDL exhibits several resonances near 1.3 kHz that were determined to be mechanical resonances within the external cavity of the laser. The measurements in Fig. 4 of the article were performed with the ECDL since the resulting displacements are well above the noise floor and the ECDL provides wider tuning range and simpler operation.

S6. Resonator Mass

The value of the proof mass in the mechanical resonator was calculated using the designed geometry and approximate densities for single-crystal silicon and the optical coatings, resulting in 11.07(53) mg for Device A and 19.59(94) mg for Device B. The main source of uncertainty in the mass is the variation in the silicon wafer thickness (±25 µm) which gives a relative uncertainty of approximately 5 % for the calculated mass. This only limits the a priori estimate of the mass, not the uncertainty of the acceleration measurement, which relies on in situ measurement of ω_0 and Q.

A similar proof mass from the same fabrication process was measured for Devices A and B after being removed from the chip. The masses were calibrated by the NIST Mass and Force Group and found to be 11.13 mg for Device A and 19.88 mg for Device B, which deviate from the calculated value by 0.5 % and 1.5 %, respectively. Any microbeams adhering to the proof mass after removal would increase the mass by less than 20 µg, and the uncertainty of the calibrated values [S2] is also negligible relative to the uncertainty of the calculated values.

S7. Uncertainties in Parameters Estimated from Fits

Fitting thermomechanical noise spectra allows ω_0, Q, and m to be measured, given the temperature. These values can vary over time due to changes in laboratory conditions, such as temperature, aging from sources including curing of packaging adhesive or accumulated stress from cycling between air and vacuum. To estimate the associated uncertainties, we use the standard deviation of multiple measurements on a device over a period of approximately eleven months. The uncertainty reported by the fitting routines is not included in the stated uncertainty as it is small compared to the variation over a year, even when accounting for variation in fitting procedures. This represents a conservative estimate for the measurements reported here. The uncertainty can be substantially reduced, for example by measuring ω_0 and Q immediately before and after acceleration measurement, but best practice for accurate acceleration metrology with the devices is outside the scope of this work and will be reported elsewhere. For Device A the relative uncertainties for ω_0, Q, and m are approximately 0.2 %, 2 %, and 8 %, respectively. Only the uncertainties in ω_0 and Q directly contribute to the uncertainty in acceleration measurement.

S8. Homodyne Interferometer

The homodyne Michelson interferometer used to test the accelerometer on a shaker table is shown in Fig. 4a from the article. A 632.8 nm stabilized HeNe laser is split into the measurement and reference arms of the interferometer using a non-polarizing 50/50 beam splitter. The light in the reference arm is reflected off of a piezoelectric-actuated mirror and light in the measurement arm is reflected off of a 5 mm square gold mirror mounted on the optomechanical accelerometer package. The reflected light from both arms interferes on a photodetector. The interferometer is locked to the quadrature point (i.e., point of highest fringe slope) using the piezoelectric mirror in the reference arm and a servo controller with a bandwidth below 100 Hz. Shaker vibrations above the servo bandwidth are measured with the interferometer and are converted to displacement using the measured fringe amplitude and laser wavelength, resulting in a noise floor of approximately 60 fm/√Hz above 1 kHz. The optomechanics for the interferometer sit on the same optical table as the shaker table, making them susceptible to vibrations driven by the shaker, as seen in the data in Fig. 4 from the article.

S9. Linearity of the Shaker Table

The comparison between the accelerometer and laser interferometer shown in Fig. 4 of the article required that the excitation amplitude of the shaker be different when using the two measurement methods. This was due to the higher sensitivity of the accelerometer relative to the interferometer by a factor of approximately 600. As a result, higher excitation amplitudes were required for detection with the interferometer. These high excitation amplitudes could not be used while reading out the microcavity in the accelerometer because the side lock could not be maintained. The end result was that measurements with the interferometer were performed with excitation amplitudes that were as much as 50 times greater than with the accelerometer readout. Due to this, the reported displacement and acceleration data are normalized by the shaker drive voltage.

This approach to the comparison is acceptable as long as the piezoelectric shaker table has a linear response for increasing excitation voltage. The linearity of the shaker table was characterized over a range of excitation voltages and frequencies, as shown in Fig. S5. The displacement of the

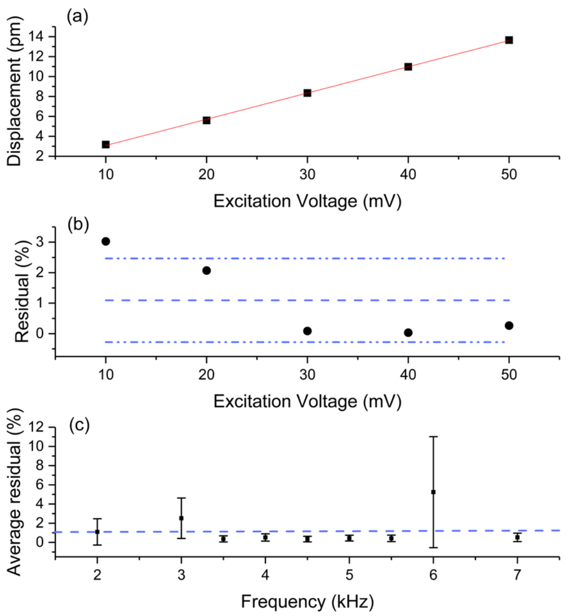

Fig. S5. Linearity of the shaker table. (a) Shaker table displacement as a function of excitation voltage at a drive frequency of 2 kHz. (b) Residuals from a linear fit to the data in (a). The residuals are an absolute value of the difference between the data and fit, expressed as a percentage of the fit value. Blue lines represent the mean (dash) and standard deviation (dash-dot) over the range of excitation voltages. (c) Mean and standard deviation residuals of the linear fit as a function of drive frequency. Blue line represents the mean over all frequencies.

shaker table for increasing excitation voltage at a single frequency (2 kHz) was found to be highly linear (Fig. S5a). The residuals for a linear fit to the data in Fig. S5a show a deviation from linearity of no more than 3 % and this deviation is much lower at higher excitation voltages due to the improved signal-to-noise ratio (Fig. S5b). Additional linearity measurements were performed between 2 kHz and 7 kHz and the mean and standard deviation of the linear fit residuals were calculated (Fig. S5c). The shaker is linear within 3 % across the entire frequency range with the exception of an outlier at 6 kHz and the mean residual is 1.1 %. This level of linearity is more than adequate for the comparison between the accelerometer and interferometer, which is discussed further in the next section.

S10. Accelerometer and Interferometer Comparison

The data in Fig. 4c of the article was analyzed to compare the results from the accelerometer and interferometer when operating on the shaker table. The deviation of the accelerometer from the interferometer was calculated as a percentage, as indicated by the blue dots in Fig. S6. A moving average filter was applied to the data from the interferometer because noise in the data was found to be a major contributor to the deviation between the two measurements. This resulted in the black line in Fig. S6, showing a significant improvement in the comparison. The deviation for the filtered data is 5.4 % ± 15.9 % (average ± standard deviation) over the entire drive frequency range (1 kHz to 20 kHz). When looking at a narrower

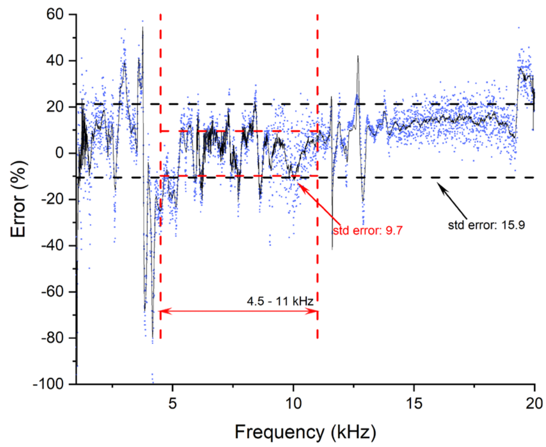

Fig. S6. Comparison of the accelerometer and interferometer results on the shaker table. Blue dots: deviation of the accelerometer results from the interferometer results. Black line: Same data set as blue dots but filtered using a moving average.

frequency range from 4.5 kHz to 11 kHz, the deviation is −0.1 % ± 9.7 %. This deviation between accelerometer and interferometer is due to a number of factors but appears to be dominated by: 1) coupling between the shaker table and optomechanics in the interferometer, 2) dynamics of the stainless-steel package, and 3) the mounting interface. Each of these will be explored in future work.

References

S1. T.W. Gabrielson, Mechanical-thermal noise in micromachined acoustic and vibration sensors, *IEEE Trans. Electron Devices* **40**, 903–909, (1993).

S2. Z. J. Jabbour, and S. L. Yaniv, The kilogram and measurements of mass and force. J. Res. Natl. Inst. Stand. Technol. **106**, 25-46 (2001).